

Spatial metrology of dopants in silicon with exact lattice site precision

M. Usman^{1*}, J. Bocquel², J. Salfi², B. Voisin², A. Tankasala³, R. Rahman³, M. Y. Simmons², S. Rogge² and L. C. L. Hollenberg^{1*}

Scaling of Si-based nanoelectronics has reached the regime where device function is affected not only by the presence of individual dopants, but also by their positions in the crystal. Determination of the precise dopant location is an unsolved problem in applications from channel doping in ultrascaled transistors to quantum information processing. Here, we establish a metrology combining low-temperature scanning tunnelling microscopy (STM) imaging and a comprehensive quantum treatment of the dopant–STM system to pinpoint the exact coordinates of the dopant in the Si crystal. The technique is underpinned by the observation that STM images contain atomic-sized features in ordered patterns that are highly sensitive to the STM tip orbital and the absolute dopant lattice site. The demonstrated ability to determine the locations of P and As dopants to 5 nm depths will provide critical information for the design and optimization of nanoscale devices for classical and quantum computing applications.

As we approach the ultimate regime of Feynman's vision¹ of nanotechnology based on atom-by-atom fabrication^{2–5}, there is a critical need to match the advances in miniaturization with atomically precise metrology. In conventional complementary metal–oxide–semiconductor⁶ and tunnelling field-effect^{7,8} transistors, the key relationship between the doping profile and performance is dominated by the positions of just a few dopant atoms, which at present cannot be quantitatively determined. Beyond conventional nanoelectronic devices, in quantum processors based on P dopants in Si^{9–17} the precise locations of the individual dopants is critical to the design and operation of spin-based quantum logic gates. Indirect approaches for locating subsurface dopant positions in Si devices can only achieve a precision of several nanometres¹⁸. Compared to previous studies on locating subsurface dopant positions in direct-bandgap semiconductors^{19,20}, the Si–dopant system is inherently more challenging due to its indirect bandgap and the presence of valley effects leading to a non-monotonic dependence of the wavefunction on dopant depth. The key metrological challenge in Si-based ultrascaled applications is determining the position of dopant atoms in the Si crystal substrate with lattice-site precision, which will drastically transform our understanding at the most fundamental scale, leading to devices with optimized functionalities.

In this Article, we present an atomically precise metrology and demonstrate the pinpointing of the position of subsurface P and As dopants in Si down to individual lattice sites. The experimental technique involves low-temperature scanning tunnelling microscopy (STM) imaging, as recently reported for As dopants in Si²¹. In ref. 21, valley interference processes were studied based on certain features of the Fourier spectra of images, which can be understood qualitatively without atomistic details of the system^{22,23}. However, precision metrology of dopant positions demands a quantitative understanding of the atomic-level details in real-space images. To meet this challenge, we have developed a fully quantum, large-volume treatment of the STM–dopant system, based on a state-of-the-art multi-million-atom tight-binding

framework^{24,25}, from which quantitative information about donor position can be extracted from STM images. We also measured STM images of P dopants with engineered depths to demonstrate the metrology procedure for both subsurface P and As dopants. A direct quantitative comparison with real-space STM images shows remarkable agreement, enabling the determination of each dopant's lattice location by uniquely reproducing the normalized tunnelling current image. The relatively large extent of the dopant electron wavefunction (Bohr radius of ~ 2 nm) as well as high-frequency content arising from the silicon valley interference processes²¹ result in the atomic-level features in the STM image, which are highly sensitive to both dopant position and details of the STM tip orbital involved. In all cases, we establish the STM tip state to be dominated by a *d*-type tip orbital, consistent with expectations for a W tip²⁶. For each experimental STM image, a quantitative comparison with the images calculated at various dopant locations allows us to uniquely pinpoint the actual three-dimensional lattice site position of the dopant with respect to the surface dimer rows for depths down to about 36 lattice planes (~ 5 nm). These results establish an STM-based metrology to determine the exact three-dimensional position of dopants in Si, as is required in modern nanoelectronics. The method is directly applicable to the fabrication of a quantum computer based on P atoms in Si⁹, and is more generally of relevance to ultrascaled nanoelectronic devices.

Figure 1 presents an overview of our metrology technique. We first describe the STM–donor measurement set-up and the quantum mechanical treatment of the tunnelling current, as shown in Fig. 1a,b. Our data set includes P (P-1 and P-2) and As (As-1 and As-2) dopants. Although the image detail has a complex relationship with the quantum mechanics of the tip orbital configuration, the tip height above the sample, the exact dopant position with regard to the lattice plane depth, and the lateral position relative to the surface dimers, we explicitly show these dependencies for a specific example (P-1). Fourier space

¹Centre for Quantum Computation and Communication Technology, School of Physics, The University of Melbourne, Parkville, 3010 Victoria, Australia.

²Centre for Quantum Computation and Communication Technology, School of Physics, The University of New South Wales, Sydney, 2052 New South Wales, Australia. ³Electrical and Computer Engineering Department, Purdue University, West Lafayette, Indiana 47907, USA.

*e-mail: musman@unimelb.edu.au; lloydch@unimelb.edu.au

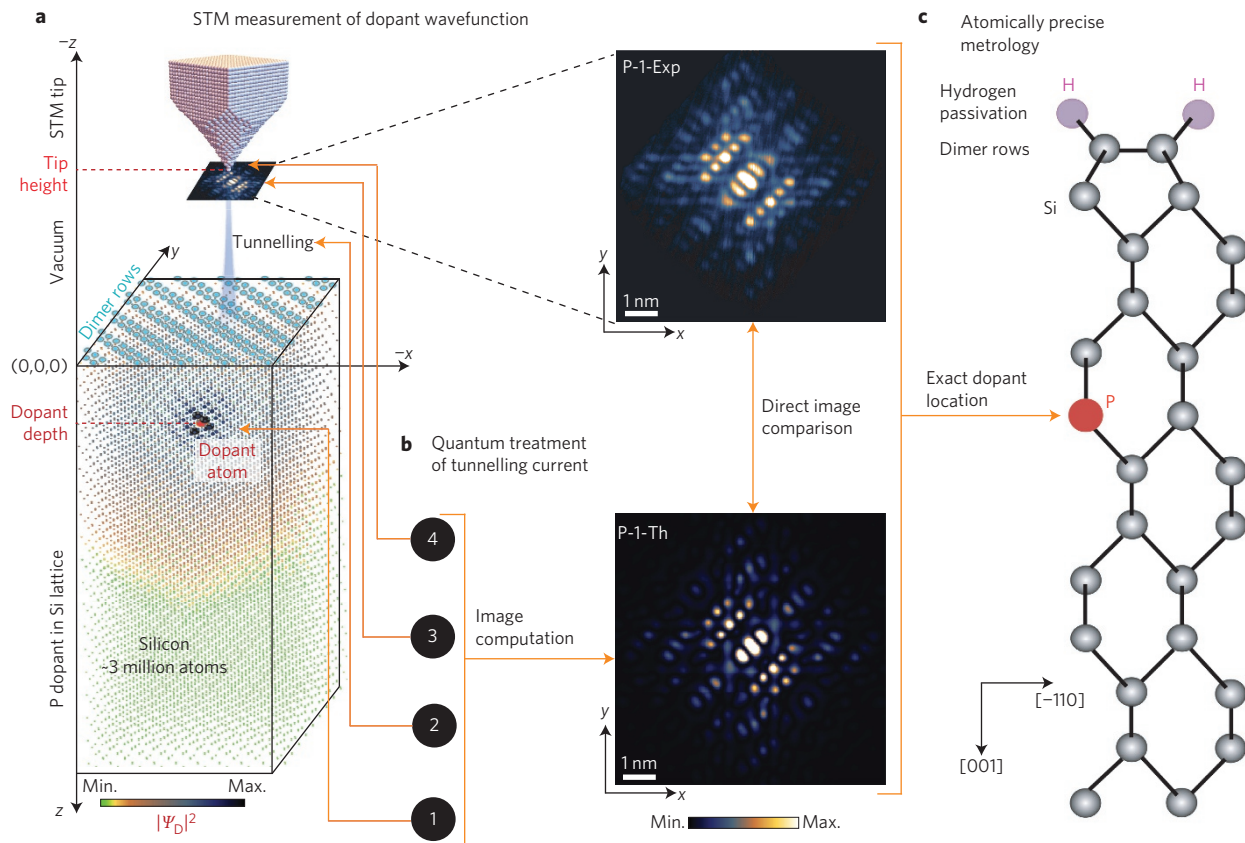


Figure 1 | STM-based metrology for the exact position of subsurface dopants in silicon. **a**, Illustration of the STM set-up used to measure atomically resolved subsurface dopant images. The dopant charge density distribution ($|\Psi_D|^2$) calculated from a tight-binding simulation over a large volume of the Si lattice is shown, colour-coded to highlight its variation as a function of distance from the dopant atom. A P dopant is positioned a few nanometres below the surface ($z=0$) and is highlighted in red. The 2×1 reconstruction results in the formation of dimer rows at the $z=0$ surface. The vertical shaded area in the vacuum region (between the sample and the STM tip) illustrates tunnelling of a single electron from the P dopant state in Si through the vacuum region to a single W atom at the STM tip apex. The measured atomically resolved image of the normalized tunnelling current is shown (P-1-Exp). The x and y axes represent [100] and [010] crystallographic directions, respectively. **b**, The theoretical framework involves the quantum mechanical treatment of the four linked components of the STM set-up, as follows: (1) multi-million atom calculation of the dopant ground-state wavefunction with 2×1 surface reconstruction ($\Psi_D(\mathbf{r})$); (2) calculation of wavefunction decay in the vacuum region ($\nabla^2 \Psi_{D,T} - \kappa^2 \Psi_{D,T}$; ref. 26); (3) determining the Bardeen tunnelling current³⁴, which is proportional to the tunnelling matrix element evaluated as a surface integral ($I \propto \int_{\chi} (\Psi_T' \nabla \Psi_D - \Psi_D \nabla \Psi_T') \cdot d\chi$) on the separation surface χ between the STM tip and the sample²⁶; and (4) establishing the STM tip state ($\Psi_T(\mathbf{r})$) from the derivative rule²⁶. The final calculated image of the normalized tunnelling current (P-1-Th) is shown. **c**, Direct quantitative comparison of the STM image and the images computed over a number of atomic positions leads to a unique identification of the subsurface dopant location in the Si lattice.

analysis provides further evidence of the correct tip orbital and surface reconstruction. By a direct quantitative (pixel-by-pixel) comparison with the experimental images (for example, as in Fig. 1c), the precise dopant position can be located with a high degree of confidence for all four members of the data set.

STM measurements of the dopant state

The electronic wavefunctions of dopants buried in a Si crystal were spatially resolved by means of low-temperature STM²¹. Both P and As dopants were measured. The P dopants were incorporated into the Si by dosing with PH_3 . A low P density was overgrown with 2.5 nm Si by *in situ* epitaxy²⁷ (that is, a target depth of $4.75a_0$, where $a_0 = 0.5431$ nm is the Si lattice constant). Careful engineering of the growth temperature profile, including for a 1 nm thin lock-in layer²⁸, gives control over the depth of the P dopants by limiting segregation and diffusion while achieving the low surface roughness required for STM measurements. The As dopants were found at random positions in an ~ 10 nm thin thermally depleted region of a highly doped substrate. All samples consist of a degenerate Si substrate acting as an electron reservoir and an intrinsic region including a low concentration of P (or As). With this vertical

sample geometry, the STM measurement falls into the single-electron transport regime²⁹. The wavefunction of electrons bound to dopants in this region was probed in real space at 5 K using a standard electrochemically etched W tip. The experimental STM images in this study (for example, P-1-Exp, shown in Fig. 1a) are normalized tunnelling current images, where the current $I(\mathbf{r})$ is proportional to $|\Im[\Psi_D(\mathbf{r})]|^2$, and \Im is a functional of the dopant wavefunction $\Psi_D(\mathbf{r})$ determined by the STM tip orbital state²⁶ (see Methods for additional details of the experimental techniques).

Quantum treatment of STM measurement

The theoretical calculation of the STM images for the subsurface dopants is challenging, because it requires an atomistic calculation of the dopant electron wavefunction over a volume comprising thousands of Si atoms, including surface reconstruction and the coupling of this description to a quantum mechanical treatment of the tip-tunnelling process. We divided the development of a theoretical framework for this problem into four stages, as shown schematically in the Fig. 1b. The first stage is the calculation of the dopant wavefunction, which is performed by solving an $sp^3d^5s^*$ atomistic tight-binding Hamiltonian³⁰ over three million

atoms, including central-cell effects^{24,25,31}, which inherently incorporates the valley-orbit (VO) interaction, to correctly capture the atomic fine detail for both P and As cases. As the dopants are close to the surface, the effects of dimer formation (2×1 reconstruction)^{23,32} and hydrogen passivation³³ are included in the tight-binding Hamiltonian (for additional details see Methods).

The STM measurements were based on the tunnelling of a single electron from the dopant ground state to the tip state through vacuum, so in the second and third stages of the theoretical framework, Bardeen's tunnelling theory³⁴ is coupled with the tight-binding dopant wavefunction to facilitate the computation of the tunnelling current and hence the image corresponding to $|\Im[\Psi_D(\mathbf{r})]|^2$ (Supplementary Section 1). The vacuum decay of the tight-binding wavefunction is based on the Slater orbital real-space dependence³⁵, which satisfies the vacuum Schrödinger equation²⁶. The exponential decay of the tunnelling current in the z direction ($I(z+dz) = I(z)e^{-2\kappa dz}$) is characterized by a decay constant κ . Our calculated values of κ in the range of 0.013–0.016 pm^{-1} for various dopant positions are in good agreement with the measured value of $\sim 0.01 \text{ pm}^{-1}$ obtained by the variation of the STM tip position. This validates the evanescent decay of the tight-binding wavefunction through the vacuum to the tip apex.

The fourth stage of the dopant image calculation involves determination of the electronic state of the STM tip, which is not known *a priori*. To comprehensively explore the role of tip orbitals and to definitively determine the tip electronic state responsible for the tunnelling current in our measurements, we start with a general tip state, described as $\Psi_T = \sum_{\beta=1}^9 A_{\beta} \phi_{\beta}^T$, where ϕ_{β}^T are $s, p_x, p_y, p_z, d_{xy}, d_{zy}, d_{zx}, d_{x^2-y^2}, d_{z^2-(1/3)r^2}$ orbitals for $\beta = 1$ to 9, respectively, with orbital weights A_{β} . The contribution from each tip orbital is based on Chen's derivative rule²⁶, in which the tunnelling current is proportional to the derivative (or the sum of derivatives) of the sample wavefunction computed at the tip location (Supplementary Section 1). Through a systematic and extensive exploration of the parameter space of the Ψ_T state (by varying A_{β}), we find a tip orbital configuration that leads to the best agreement with the experimental measurement. This procedure necessarily involves a rigorous search through physical parameters such as dopant depth, dopant position underneath the dimer rows and tip height above the Si surface. Finally, a quantitative comparison of the measured and calculated images is performed by defining two comparator parameters: pixel-by-pixel difference (C_p) and feature-by-feature correlation (C_f) of the images (Supplementary Section 1).

STM tip state and surface reconstruction

Figure 1b presents the final (normalized) theoretical STM image for the P dopant P-1. The final converged images for three other dopants (P-2, As-1 and As-2) are shown in Supplementary Fig. 7, together with the corresponding STM measurements, all of which exhibit excellent agreement between theory and experiment. In the computation of the images, the unknown physical quantities related to the STM measurement set-up form a large parameter space to explore. In general, these include the tip orbital configuration (Ψ_T), the height of the tip above the $z = 0$ surface, the depth of the dopant atom below the $z = 0$ surface, and the position of the dopant atom with respect to the surface dimer rows. This complex problem space is systematically tackled to obtain the optimal agreement between theory and experiment. We first focus on how varying those parameters affects the images, using dopant P-1 as an example.

By using the generalized tip state and optimizing the tip orbital weights A_{β} , we can study the dopant images as a function of the tip orbital configuration. To illustrate the effect of the tip orbital on the calculated images, Fig. 2 presents theoretical images for dopant P-1 at a depth of $4.75a_0$ and a tip height of 2.5 \AA as a function of individual tip orbitals. Evidently, each tip orbital captures a very different symmetry of the same dopant wavefunction. Referring to the experimental image (P-1-Exp) in Fig. 1b, the character of the image is

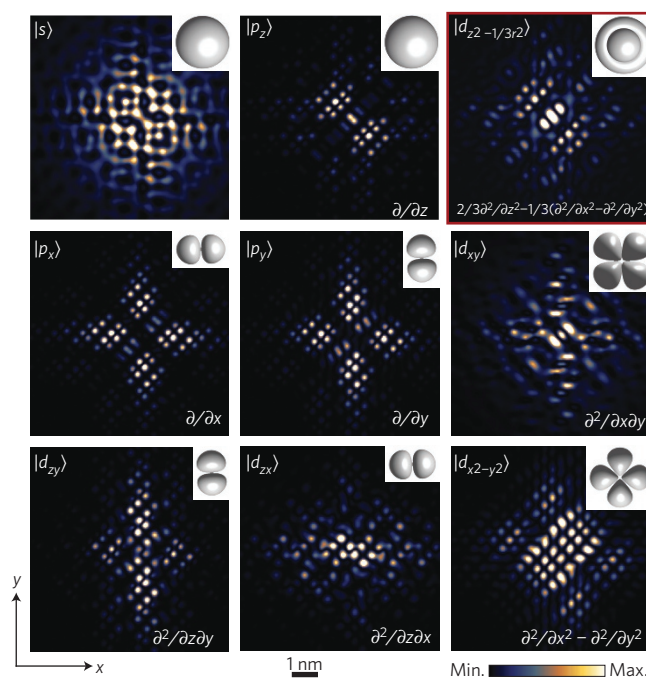


Figure 2 | STM tip orbital dependence. Theoretically computed $|\Im[\Psi_D(\mathbf{r})]|^2$ images for the P-1 dopant as a function of the individual orbitals in the STM tip state (Ψ_T). Each image is labelled by the corresponding tip orbital (top left of each image), the corresponding orbital symmetry in the x - y plane (top right of each image) and the differential operator based on Chen's derivative rule²⁶ applied to the sample wavefunction (bottom right of each image). Note that an s tip orbital will give an image directly proportional to the modulus squared of the wavefunction, without any derivative. The tip height is taken to be 2.5 \AA and the dopant depth is $4.75a_0$. Each tip orbital produces a very different image of the dopant wavefunction, and only the $d_{z^2-(1/3)r^2}$ orbital image (highlighted by the red border) captures the symmetry of the atomic features present in the measured data P-1-Exp shown in Fig. 1b.

clearly dominated by the $\Psi_T = d_{z^2-(1/3)r^2}$ tip state. For all the measured P and As images, we consistently find that the $d_{z^2-(1/3)r^2}$ orbital in the tip state is by far (more than 90%) the most dominant contribution, theoretically reproducing the symmetry of the measured images (Supplementary Fig. 7). This is consistent with the existing arguments based on density of states^{26,36,37}, which suggest that d -type orbitals should dominantly contribute in the tunnelling currents involving STM tips composed of transition-metal elements. The quantitative agreement between our measurements and theory therefore provides a concrete verification of the dominant d -wave tunnelling. In our case, the major contribution is from the $d_{z^2-(1/3)r^2}$ orbital. We are able to infer this because of the presence of high-frequency components arising from the valleys of the Si-dopant system and the unusually large spatial extent of the wavefunction (compared to the atomic-sized features) of dopants below the surface, which are highly sensitive to the precise tip orbital configuration. In Supplementary Fig. 5, we compare the Fourier transform spectra (FTS) of the measured and calculated images for the P-1 dopant. The excellent agreement confirms the dominant role of the $d_{z^2-(1/3)r^2}$ orbital in tunnelling current and the 2×1 surface reconstruction scheme.

Pinpointing the exact dopant location

Having validated the tip orbital and surface reconstruction, we next demonstrate how the depth and lateral position of the dopant with respect to the surface dimers have a significant effect on the image symmetry and ultimately permit the identification of the actual dopant lattice site. Supplementary Fig. 8 presents a schematic

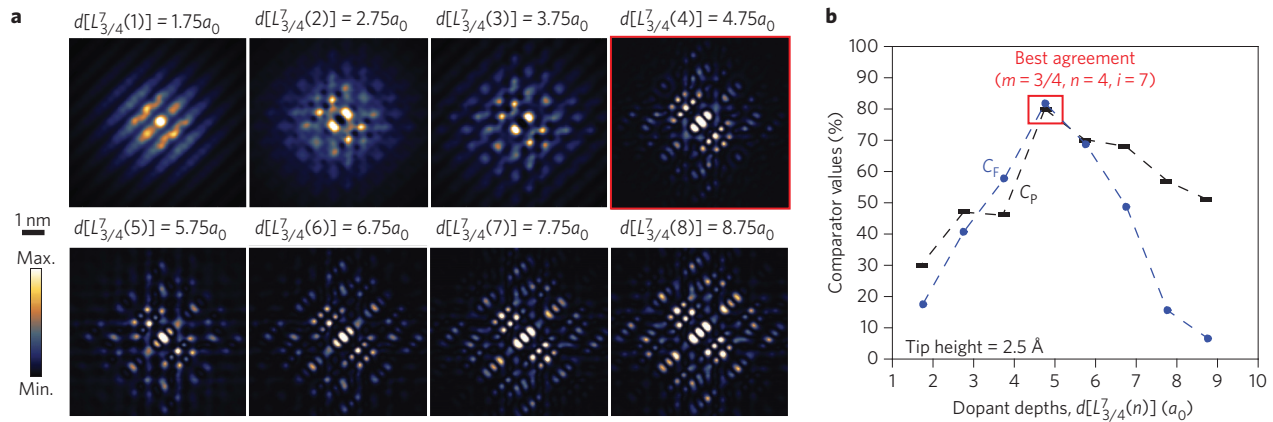


Figure 3 | Unique lattice site assignment for the P-1 dopant by depth analysis. **a**, To identify the exact location of the measured P-1-Exp image, theoretically computed images are shown as a function of plane depth n once the $L_{3/4}^7(n)$ location group has been identified from the image symmetry (for details see Supplementary Fig. 4). The computed image at a depth of $4.75a_0$ (highlighted by the red border), corresponding to $n=4$, exhibits the best quantitative agreement with the measured P-1-Exp image, as is evident from the comparator peaks. **b**, Plot of pixel-by-pixel C_P and feature-by-feature C_F comparators between the P-1-Exp image and the theoretical images in **a**. The best agreement with the P-1-Exp image is uniquely identified at a dopant depth of $4.75a_0$ ($m=3/4, n=4, i=7$) by the joint peaks of both comparator parameters. The corresponding depth plane analyses for the other dopants in the set (P-2-Exp, As-1-Exp and As-2-Exp) are shown in Supplementary Fig. 9.

diagram of the Si crystal, establishing our notation regarding the possible donor positions below the surface. Along the [001] direction, each lattice position corresponds to a unique depth and therefore should lead to a distinct image. A closer examination of the dopant images uncovers subtle symmetry effects, which repeat for every fourth plane. The Si lattice planes are therefore divided into four plane groups (PG_m , where $m \in \{0, 1/4, 1/2, 3/4\}$). Each plane group is a set of planes $P_m(n)$, whose depths from the $z=0$ surface are given by $d[P_m(n)] = (m+n)a_0$, where $n=0, 1, 2, 3, \dots$. Note that $(m, n) = (0, 0)$ corresponds to the $z=0$ surface. Considering the periodicity of the dimers along the $[-110]$ direction, two possible dopant locations $L_m^i(n)$ per plane $P_m(n)$ are defined by $i=8m+1$ and $i=8m+2$, which repeat periodically in the lateral direction. The dopant locations $L_m^i(n)$ are colour coded in Supplementary Fig. 8 with respect to the dimer rows, and the eight positions marked as $i=1$ to 8 periodically repeat in all crystal directions. The positions $i=1$ & 2 and 3 & 4 (coloured blue) are below the edges of the dimer rows and therefore are equivalent; at a given depth n , dopants at locations 1 and 3 will lead to the same image features as locations 2 and 4, respectively, with 180° rotation. The allocation of the exact dopant site (1 or 2, 3 or 4) is based on the overlying dimer positions on top of the image and finding the dopant location on either edge of the dimers. Overall, the classification with respect to the unique patterns of image features leads to six possible distinguishable dopant location-groups in the Si lattice, which are given by $L_0^{1,2}(n)$, $L_{1/4}^{3,4}(n)$, $L_{1/2}^5(n)$, $L_{1/2}^6(n)$, $L_{3/4}^7(n)$ and $L_{3/4}^8(n)$. For an experimental STM image, our metrology technique first associates it with one of the six location-groups (by determining m and i), followed by a quantitative depth comparison of images within that group (by varying n).

The assignment of a location-group to a measured STM image is based on a systematic procedure derived from careful analysis of the symmetries of the image features. The details of the procedure are described in Supplementary Section 2, as well as its application to the four measured STM images. After determining a location-group for the measured image (for example $L_{3/4}^7(n)$ location-group for the P-1-Exp image), we next quantitatively compare the computed images within the allocated location-group with the measured image by varying the plane depth n . Figure 3a presents an analysis for the P-1-Exp image where n is varied from 1 to 8. The corresponding comparator graphs (C_P and C_F) between each theory and P-1-Exp image are plotted in Fig. 3b. The highest comparator

values ($C_P=80\%$ and $C_F=82\%$) uniquely locate the P dopant at position $L_{3/4}^7(4)$ ($4.75a_0$ depth), as plotted in Fig. 4a. To include the effect of tip height variation in the theoretical calculation and/or instabilities of the tip height in the measurements, we changed the 2.5 Å tip height by ± 0.125 Å and recomputed the values of C_P and C_F for $n=4$. This $\pm 5\%$ tip height variation introduced only small changes in the comparator values (less than 2%), indicating that such an effect is not expected to influence the optimum agreement between theory and experiment for the dopant location of $L_{3/4}^7(4)$, computed with the $d_{z^2-(1/3)r^2}$ wave tip.

The application of the procedure to the other dopants in the data set—P-2-Exp, As-1-Exp and As-2-Exp—gave a similar behaviour for the respective comparators (Supplementary Fig. 9), allowing us to uniquely identify their positions. The final results for the positions and computed images for the whole data set are shown in Fig. 4. We should emphasize here that the existence of the peak in the comparator graphs is more meaningful than the value itself, as the measurements include some invariably present perturbations to the dopant wavefunction that have not been considered in the model. In general, these perturbations include applied electrostatic potentials from the STM tip itself and background electrostatic disorder, which is an aggregate of charge density disorder in the buried reservoir and nearby (>10 nm away) dangling bonds. As discussed in refs 21 and 29, we can control the tip-induced band bending during dopant state measurements and, as desired in the present work, we minimize the potential applied by the STM tip. The residual fields are typically on the order of 2 MV m^{-1} (ref. 29) and thus are much smaller than those predicted to hybridize the dopant wavefunction with an interface-well wavefunction³⁸. Furthermore, Bardeen's first-order tunnelling approach³⁴ does not take into account the higher-order tip-induced modifications to the wavefunction. It is remarkable that despite these simplifications in the model, both C_P and C_F comparator peaks coexist at the same dopant location, with values exceeding 60%, indicating a high-level feature-by-feature match between the measured and computed images (Supplementary Fig. 7), enabling the unambiguous pinpointing of the exact dopant lattice site position in each of the four data sets.

The comparison for the deepest dopant As-2 (Fig. 4e) shows that the procedure is reaching its limit at a depth of $9a_0$, corresponding to the 36th lattice planes below the $z=0$ surface. We also note that a comparison of the computed P and As images revealed large differences at small dopant depths ($3a_0$ or less), which drastically decrease

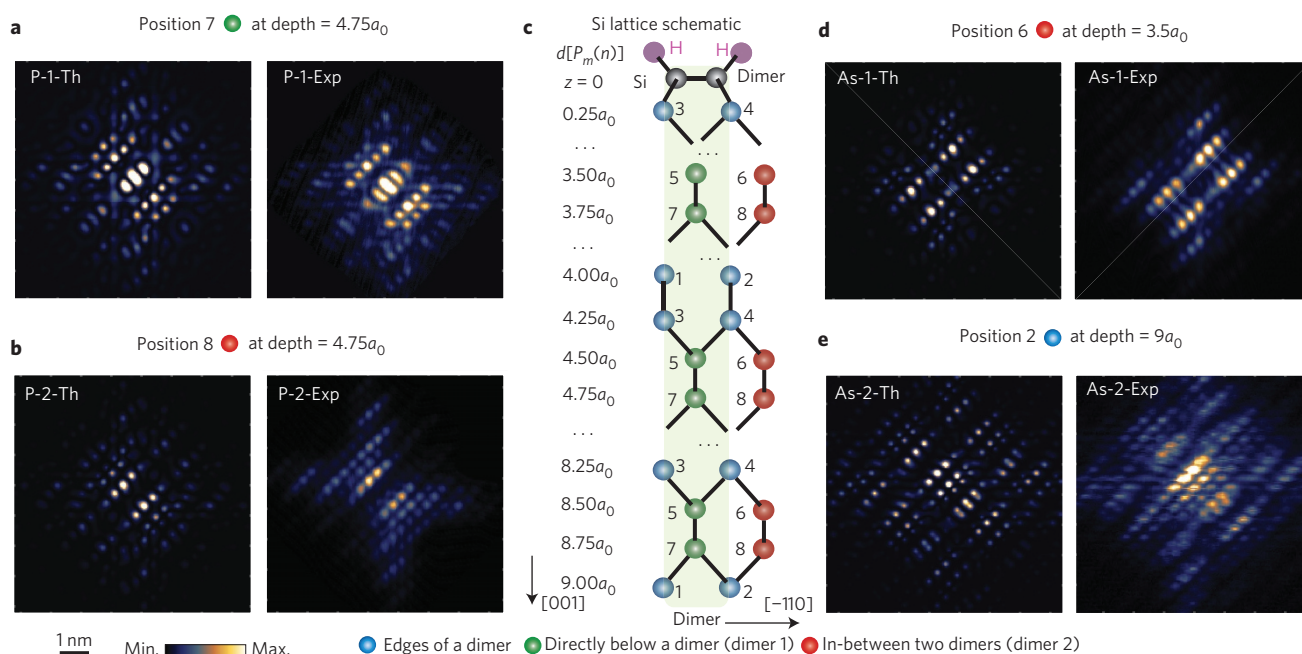


Figure 4 | Pinpointing dopant location with single-lattice-site precision. **a,b**, Theoretically computed and experimentally measured images (normalized equivalently) for dopants P-1 (**a**) and P-2 (**b**) at final determined lattice site positions $L_{3/4}^6(4)$ and $L_{3/4}^8(4)$ (depth = $4.75a_0$), respectively. Despite being at the same depth from the $z = 0$ surface, the symmetries of the P-1 and P-2 images reflect the different positions relative to the surface dimer rows (directly underneath the dimer and between the two dimer rows, respectively). The location of the dopants is therefore uniquely determined in terms of depth and with respect to the surface dimer positions. **c**, Illustration of the relevant Si lattice sites in the Si crystal structure. The topmost surface of the Si is hydrogen passivated (H atoms are shown in purple). At the $z = 0$ surface, dimer rows are shown along the direction perpendicular to the page (indicated by the atoms in grey). The three categories of lattice positions are shown as blue, green and red atoms with respect to the dimer rows: green = positions directly below the dimer rows, red = positions between two dimer rows, and blue = positions at the edges of a dimer row. Due to symmetry properties, green and red positions would correspond to unique patterns of features in the images, whereas blue positions simply lead to 180° rotation of the image features. **d,e**, Theoretically computed and experimentally measured images (normalized equivalently) are shown for dopants As-1 (**d**) and As-2 (**e**) at final determined lattice site positions $L_{1/2}^6(3)$ (depth = $3.5a_0$) and $L_0^2(9)$ (depth = $9a_0$), respectively.

as the dopant positions get deeper. This is expected, as the P and As wavefunctions primarily differ in their central-cell effects, which are tightly confined closer to the dopant atoms. A comparison of Fig. 4a and b highlights the effect of the surface reconstruction, which results in drastically different spatial symmetries of the images despite the corresponding P dopants being at the same $4.75a_0$ depth from the $z = 0$ surface. On the contrary, the FTS of these two images (Supplementary Fig. 6a,b) do not differ in any great detail. This implies that although the position of the dopant with respect to dimers is crucial in determining the symmetry of STM-measured images, it has very little impact on the actual dopant wavefunction and its underlying valley configuration. The impact of the lateral surface strain due to the 2×1 reconstruction is found to be very weak for the valley configurations, which are primarily governed by the depth of the dopant along the [001] axis. This is confirmed by comparing the calculated valley populations for the P-1 and P-2 dopants, which differ by less than 0.1%, compared to $\sim 1.25\%$ change if P-1 at $4.75a_0$ depth is compared to a P dopant at $4.5a_0$ depth. Finally, it is interesting to note that the metrology of both P dopants reveals their depths to be $4.75a_0$, which coincides with the incorporated target depth. Indeed, this metrology now allows assays to be performed that could determine whether this is really indicative of low segregation during the fabrication process.

Summary and outlook

Our STM measurements in conjunction with large-scale quantum simulations provide an atomic-precision metrology procedure for determining the exact locations of subsurface group V dopants in Si. The large Bohr radius of the dopant electron (compared with

the Si lattice constant) provides a rich variety of atomic-sized features in the STM images, the symmetry and details of which are highly sensitive to the absolute position of the dopant below the surface. In the atom-by-atom fabrication of nanoscale electronic devices more generally, the determination of the precise positions of countable dopants is critical to device performance and is expected to lead to optimization strategies for fabrication and characterization. The critical role of the STM tip state in our measurements is established, which is necessary to understand both the real and Fourier space spectra of the dopant wavefunction from STM images (Supplementary Section 3). The high-level agreement between theory and experiment achieved here for the normalized tunnelling current images can be pushed further to understand hitherto hidden subtle effects such as central-cell corrections at the dopant site, local strain conditions, surface effects, valley interference and non-static screening of the dopant electron in the Si crystal. Precision metrology of dopant locations in the fabricated closely spaced dopant pairs³⁹ will enable probing of multiparticle physics and provide an ideal testbed to answer fundamental questions pertaining to molecular physics. The method could be used in the development of ultrascaled Si nanoelectronics and for locating dopants in other indirect-bandgap material systems such as Ge:P. For quantum computer architectures⁹, with the exact relative dopant qubit distances known during the fabrication stage, highly precise quantum logic gates can be constructed—a fundamental ingredient for quantum error correction and scale-up.

Methods

Methods and any associated references are available in the [online version of the paper](#).

Received 22 December 2015; accepted 18 April 2016;
published online 6 June 2016

References

- Ball, P. Feynman's fancy. *Chem. World* **58**, 58–62 (2009).
- Fuechsle, M. *et al.* A single atom transistor. *Nature Nanotech.* **7**, 242–246 (2012).
- Weber, B. *et al.* Ohm's law survives to the atomic scale. *Science* **335**, 64–67 (2012).
- Ho, J. *et al.* Controlled nanoscale doping of semiconductors via molecular monolayers. *Nature Mater.* **7**, 62–67 (2008).
- Prati, E. & Shinada, T. *Single-Atom Nanoelectronics* (Pan Stanford, 2013).
- Pierre, M. *et al.* Single-donor ionization energies in a nanoscale CMOS channel. *Nature Nanotech.* **5**, 133–137 (2010).
- Sarkar *et al.* A subthermionic tunnel field-effect transistor with an atomically thin channel. *Nature* **526**, 91–95 (2015).
- Ionescu *et al.* Tunnel field-effect transistors as energy-efficient electronic switches. *Nature* **479**, 329–337 (2011).
- Hill, C. *et al.* A surface code quantum computer in silicon. *Sci. Adv.* **1**, e1500707 (2015).
- Kane, B. E. A silicon-based nuclear spin quantum computer. *Nature* **393**, 133–137 (1998).
- Saeedi, K. *et al.* Room-temperature quantum bit storage exceeding 39 minutes using ionized donors in silicon-28. *Science* **342**, 830–833 (2013).
- Pla, J. *et al.* High-fidelity readout and control of a nuclear spin qubit in silicon. *Nature* **496**, 334–338 (2013).
- Muhonen, J. T. *et al.* Storing quantum information for 30 seconds in a nanoelectronic device. *Nature Nanotech.* **9**, 986–991 (2014).
- Weber, B. *et al.* Spin blockade and exchange in coulomb-confined silicon double quantum dots. *Nature Nanotech.* **9**, 430–435 (2014).
- Tyryshkin, A. *et al.* Electron spin coherence exceeding seconds in high-purity silicon. *Nature Mater.* **11**, 143–147 (2012).
- Dehollain, J. P. *et al.* Bell's inequality violation with spins in silicon. *Nature Nanotech.* **11**, 242–246 (2016).
- Laucht, A. *et al.* Electrically controlling single-spin qubits in a continuous microwave field. *Sci. Adv.* **1**, e1500022 (2015).
- Mohiyaddin, F. *et al.* Noninvasive spatial metrology of single-atom devices. *Nano Lett.* **13**, 1903–1909 (2013).
- Garleff, J. K. *et al.* Atomically precise impurity identification and modification on the manganese doped GaAs(110) surface with scanning tunneling microscopy. *Phys. Rev. B* **78**, 075313 (2008).
- Marczinowski, F. *et al.* Effect of charge manipulation on scanning tunneling spectra of single Mn acceptors in InAs. *Phys. Rev. B* **77**, 115318 (2008).
- Salfi, J. *et al.* Spatially resolving valley quantum interference of a donor in silicon. *Nature Mater.* **13**, 605–610 (2014).
- Saraiva, A. L. *et al.* Donor wave functions in Si gauged by STM images. *Phys. Rev. B* **93**, 045303 (2015).
- Klymenko, M. V. *et al.* Multivalley envelope function equations and effective potentials for phosphorus impurity in silicon. *Phys. Rev. B* **92**, 195302 (2015).
- Usman, M. *et al.* Strain and electric field control of hyperfine interactions for donor spin qubits in silicon. *Phys. Rev. B* **91**, 245209 (2015).
- Rahman, R. *et al.* High precision quantum control of single donor spins in silicon. *Phys. Rev. Lett.* **99**, 036403 (2007).
- Chen, C. J. Tunneling matrix elements in three-dimensional space: the derivative rule and the sum rule. *Phys. Rev. B* **42**, 8841 (1990).
- Miwa, J. A., Mol, J. A., Salfi, J., Rogge, S. S. & Simmons, M. Y. Transport through a single donor in p-type silicon. *Appl. Phys. Lett.* **103**, 043106 (2013).
- Keizer, J. G. *et al.* The impact of dopant segregation on the maximum carrier density in Si:P multilayers. *ACS Nano* **9**, 7080–7084 (2015).
- Voisin, B., Salfi, J., Bocquel, J., Rahman, R. & Rogge, S. Spatially resolved resonant tunneling on single atoms in silicon. *J. Phys. Condens. Matter* **27**, 154203 (2015).
- Boykin, T. B., Klimeck, G. & Oyafuso, F. Valence band effective-mass expressions in the $sp^3d^5s^*$ empirical tight-binding model applied to a Si and Ge parametrization. *Phys. Rev. B* **69**, 115201 (2004).
- Usman, M. *et al.* Donor hyperfine Stark shift and the role of central-cell corrections in tight-binding theory. *J. Phys. Condens. Matter* **27**, 154207 (2015).
- Craig, B. I. & Smith, P. V. The structure of the Si(100) 2×1 : H surface. *Surf. Sci.* **226**, L55–L58 (1990).
- Lee, S., Oyafuso, F., von Allmen, P. & Klimeck, G. Boundary conditions for the electronic structure of finite-extent embedded semiconductor nanostructures. *Phys. Rev. B* **69**, 045316 (2004).
- Bardeen, J. Tunneling from a many-particle point of view. *Phys. Rev. Lett.* **6**, 57 (1961).
- Slater, J. C. Atomic shielding constants. *Phys. Rev.* **36**, 57 (1930).
- Chaika, A. N. *et al.* Selecting the tip electron orbital for scanning tunneling microscopy imaging with sub-angstrom lateral resolution. *Eur. Phys. Lett.* **92**, 46003 (2010).
- Teobaldi, G., Inami, E., Kanasaki, J., Tanimura, K. & Shluger, A. L. Role of applied bias and tip electronic structure in the scanning tunneling microscopy imaging of highly oriented pyrolytic graphite. *Phys. Rev. B* **85**, 085433 (2012).
- Rahman, R. *et al.* Engineered valley-orbit splittings in quantum-confined nanostructures in silicon. *Phys. Rev. B* **83**, 195323 (2011).
- Salfi, J. *et al.* Quantum simulation with dopant atoms in a semiconductor. *Nature Commun.* **7**, 11342 (2016).

Acknowledgements

This work is funded by the Australian Research Council Center of Excellence for Quantum Computation and Communication Technology (CE110001027) and in part by the US Army Research Office (W911NF-08-1-0527). M.Y.S. acknowledges an ARC Laureate Fellowship. This work is supported by the European Commission Future and Emerging Technologies Proactive Project MULTI (317707). Computational resources are acknowledged from NCN/Nanohub. M.U. thanks C. Hill and V. Perunicic for discussions.

Author contributions

L.C.L.H. and M.U. formulated the theoretical framework for the metrology scheme, including tight-binding calculations of the STM images with generic tip orbitals with input from J.S. M.U. performed the theoretical calculations. J.B., J.S., B.V., M.Y.S. and S.R. designed and conducted the STM measurements. L.C.L.H. and M.U. wrote the manuscript with input from all authors.

Additional information

Supplementary information is available in the [online version of the paper](#). Reprints and permissions information is available online at www.nature.com/reprints. Correspondence and requests for materials should be addressed to M.U. and L.C.L.H.

Competing financial interests

The authors declare no competing financial interests.

Methods

Sample preparation. Two different types of sample, with either P or As dopants, were prepared in ultrahigh vacuum (UHV) within a low-temperature STM system. Samples with As dopants were prepared by flash annealing a 0.003 Ω cm As-doped wafer three times at $\sim 1,050^\circ\text{C}$ for a total of 30 s. Under these conditions, a layer ~ 10 nm from the Si surface is depleted, leaving an As concentration of $\sim 2 \times 10^{17} \text{ cm}^{-3}$ (ref. 21). Consequently, As dopants measured in these samples were found at random depths in a ~ 10 nm thin thermally depleted Si layer below the surface. Samples with P dopants were prepared by incorporating P in Si by submonolayer phosphine (PH_3) dosing of the previously flash-annealed Si substrate²⁷. A sheet density of $5 \times 10^{11} \text{ cm}^{-2}$ P donors was overgrown epitaxially by ~ 2.5 nm Si ($4.75a_0$, where a_0 is the Si lattice constant). The first nanometre is a lock-in layer grown at room temperature²⁸, and growth parameters such as temperature and flux were chosen to achieve minimal segregation and diffusion. Consequently, the depth of P donors was controlled. The 2×1 -reconstructed Si (001) surface of all samples was passivated with H. H termination was carried out at $T = 340^\circ\text{C}$ for ~ 10 min under a flux of atomic H produced by a thermal cracker, in a chamber with a 10^{-7} mbar pressure of molecular hydrogen. In both P- and As-doped samples, consisting of a degenerate Si substrate acting as an electron reservoir and an intrinsic region including a low concentration of donors, the STM measurement falls into the single-electron transport regime described in ref. 29. A schematic of this vertical structure and the STM junction is shown in Fig. 1a.

Spatially resolved transport measurements. The samples were measured by STM and spectroscopy at 4.2 K in UHV using an electrochemically etched W tip. We observed spatially localized states in constant-current images at a nominal sample bias of $U = -1.25$ V and a tunnel current 100 pA. The spatially localized features resolved into a series of single-electron transport peaks in bias-resolved tunnelling spectroscopy^{21,29,40}. The lowest-energy state of a donor was measured with high resolution in real space using an unconventional two-pass scheme, where the topography was first measured at $U = -1.45$ V. Replaying the topography in the second pass, we measured the current in open-loop mode, typically at a bias $U = -0.8$ V, where only the neutral donor state is in the bias window and there was a constant tip offset of 200 pm towards the sample to enhance the tip–donor coupling. Owing to complex valley quantum interference processes observed upon Fourier transformation of the measured state and supported by the state's proximity to the empirically determined flat-band condition, the lowest energy state was attributed to transport through the ground state of the neutral donor charge configuration²¹. The broadening of the lowest energy peak is always essentially independent of tip height, and the transport line shape matches what is expected for broadening due to coupling to a thermally broadened Fermi sea⁴¹ at liquid He temperature. We attribute this to weak tunnel coupling of the donor to a buried Fermi sea, as expected for flash-annealed Si substrates⁴².

Independent donor depth estimation for As-1 data. The depth of a dopant beneath a semiconductor surface can be estimated by comparing measurements of the spatial perturbation of a feature such as a band edge by the ionized dopant, based on a comparison of spectroscopic data to an electrostatic model. One such model, first used for dopants in GaAs^{43,44}, is based on a dielectric screened Coulomb potential with a discontinuity at the semiconductor/vacuum interface. This model has recently been applied to single acceptors⁴⁰ and donors²¹ in Si. Following ref. 21, we used this method to estimate the depth of the As-1-Exp donor. To do so, we measured the spatial variation of the onset of the conduction band edge at a positive sample bias of $U > 0$, well above the flat-band condition $U \approx -0.8$ V, where the neutral donor state is above the Fermi energy of the highly doped reservoir. The sample bias U_C required to obtain a tunnel current of 0.1 pA was spatially mapped in two dimensions (x, y) as a function of position, and fitted to a Coulomb potential for the donor As-1-Exp. We obtained a depth of $z_0 = (5 \pm 1)a_0$ nm, which, in spite of assuming a static dielectric constant for Si and ignoring the screening of the ion potential induced by the metallic STM tip, is reasonably close to the $3.5a_0$ depth determined by our metrology.

Electric field measurement. This section presents experimental procedures to extract quantitative parameters such as tip height variations and electric fields at the donor site, following refs 21 and 29. The electric field experienced by the donor bound electron during the measurement is determined by measurements of the tunnelling spectrum taken with different tip heights. We compare these measurements to a one-dimensional model for electrostatics. Under the flat-band condition, there is no electric field present in the vacuum and, following simple

electrostatic arguments, the bias required to bring the state into resonance with the reservoir is independent of tip height. However, when there is a non-zero electric field in vacuum, a small change in bias is required to bring the state into resonance when the tip height is changed. From the required bias and change in tip height we can quantitatively extract the field in vacuum and, using a simple model for dielectric screening, the electric field in the Si. Typical values of electric fields experienced by donors, when imaged in resonant conditions, are less than 2 MV m^{-1} in magnitude.

The tip height variations discussed in this section were calibrated to the height of step edges on the Si (001) surface, which are a quarter of the cubic lattice constant of Si. However the absolute tip height cannot be quantitatively estimated, as it depends on the exact barrier and tip shapes, and the resulting coupling with the donor evanescent wavefunction, quantities that cannot be precisely determined at such small length scales. Offsets of 200 to 300 pm are typically used during the second pass. Larger offsets towards the surface can bring the tip into contact with the surface.

Multi-million-atom calculation of dopant wavefunction. The atomistic simulations of electronic energies and states for a dopant in Si were performed by solving an $sp^3d^5s^*$ tight-binding Hamiltonian. The $sp^3d^5s^*$ tight-binding parameters for the Si material were obtained from ref. 30, and have been optimized to accurately reproduce the Si bulk band structure. The dopant atoms (P and As) are represented by a Coulomb potential screened by the non-static dielectric of the Si^{24,31}, truncated to $U(r_0) = U_0$ at the dopant site (r_0). Here, U_0 is an adjustable parameter that represents the central-cell correction and has been designed to accurately match the ground-state binding energies of the P and As dopants as measured in the experiment^{25,45}. The size of the simulation domain (Si box around the dopant) is chosen as 40 nm^3 , consisting of roughly three million atoms, with closed boundary conditions in all three spatial dimensions. The effect of hydrogen passivation on the surface atoms is implemented in accordance with our published procedure³³, which shifts the energies of the dangling bonds to avoid any spurious states in the energy range of interest. The multi-million-atom real-space Hamiltonian is solved by a parallel Lanczos algorithm to calculate the single-particle energies and wavefunctions of the dopant atom. The tight-binding Hamiltonian is implemented within the framework of NEMO 3-D⁴⁶.

In our experiments, the (001) sample surface consisted of dimer rows of Si atoms. We incorporated this effect into our atomistic theory by implementing a 2×1 surface reconstruction scheme, in which the surface Si atoms were displaced in accordance with published studies^{21,32}. The impact of the surface strain due to the 2×1 reconstruction was included in the tight-binding Hamiltonian by a generalization of Harrison's scaling law³⁰, where the inter-atomic interaction energies are modified with the strained bond length d as $(d_0/d)^\eta$, where d_0 is the unperturbed bond length of the Si lattice and η is a scaling parameter whose magnitude depends on the type of interaction being considered and is fitted to obtain hydrostatic deformation potentials. It is emphasized here that the atomistic nature of our model has allowed a straightforward implementation of the surface reconstruction effect in our simulations, which would be inaccessible in continuum models based on effective-mass theories^{22,23}.

Additional methods regarding the STM image calculations and the Fourier transform analysis are provided in the Supplementary Information.

References

- Mol, J. A., Salfi, J., Miwa, J. A., Simmons, M. Y. & Rogge, S. S. Interplay between quantum confinement and dielectric mismatch for ultrashallow dopants. *Phys. Rev. B* **87**, 245417 (2013).
- Averin, D., Korotkov, A. & Likharev, K. Theory of single-electron charging of quantum wells and dots. *Phys. Rev. B* **44**, 6199–6211 (1991).
- Pitters, J. L., Piva, P. G. & Wolkow, R. A. Dopant depletion in the near surface region of thermally prepared silicon (100) in UHV. *J. Vac. Sci. Technol. B* **30**, 021806 (2012).
- Lee, D.-H. & Gupta, J. A. Tunable field control over the binding energy of single dopants by a charged vacancy in GaAs. *Science* **330**, 1807–1810 (2010).
- Teichmann, K. *et al.* Controlled charge switching on a single donor with a scanning tunneling microscope. *Phys. Rev. Lett.* **101**, 076103 (2008).
- Ahmed, S. *et al.* in *Encyclopedia of Complexity and Systems Science* (ed. Meyers, R.) 5745–5783 (Springer, 2009).
- Klimeck, G. *et al.* Atomistic simulation of realistically sized nanodevices using NEMO 3-D—part II: Models and benchmarks. *IEEE Trans. Electron. Dev.* **54**, 2090–2099 (2007).